Design optimization of turbine flow meter in ice maker water supply to improve flow measurement performance

Citation for the original published paper (version of record):
Kim, H., Cheong, C., Ryu, S. et al (2026). Design optimization of turbine flow meter in ice maker water supply to improve flow measurement performance. Flow Measurement and Instrumentation, 108. http://dx.doi.org/10.1016/j.flowmeasinst.2025.103134

Flow Measurement and Instrumentation 108 (2026) 103134

Contents lists available at ScienceDirect

Flow Measurement and Instrumentation

journal homepage: www.elsevier.com/locate/flowmeasinst

Design optimization of turbine flow meter in ice maker water supply to improve flow measurement performance

Haechan Kim [a], Cheolung Cheong [a,b,*], Seo-Yoon Ryu [c], Su Il Park [d]

[a] School of Mechanical Engineering, Pusan National University, 46241, Busan, South Korea
[b] Center for Advanced Air-conditioning, Refrigeration & Energy, Pusan National University, 46241, Busan, South Korea
[c] School of Mechanics and Maritime Sciences, Chalmers University of Technology, SE-412 96, Gothenburg, Sweden
[d] LG Electronics, Changwon 2nd Factory, Seongsan-gu, Gyeongsangnam-do, 51555, Changwon-si, South Korea

ARTICLE INFO

Keywords:
Turbine flow meter
K-factor
Flow measurement performance evaluation
Design optimization
FSI simulations

ABSTRACT

This paper aims to improve the flow measurement performance of a turbine flow meter used in a refrigerator ice maker, especially under low-pressure conditions, where nonlinear characteristics lead to diminished measurement accuracy. Accordingly, we associate defects in spherical-ice quality with metering errors caused by the low-pressure K-factor nonlinearity of the tangential-type turbine flow meter. To this end, an experimental calibration system for the flow meter was designed and constructed, and the reliability of its experimental data was verified using the flow calibration apparatus provided by the Korea Research Institute of Standards and Science (KRISS). Based on this experimental system, a response surface for finding the optimal impeller design of the turbine flow meter was developed using the Design of Experiments (DOE) methodology. To minimize the nonlinear region of the K-factor under low-pressure conditions and the standard deviation of the K-factor under high-pressure conditions, the transition location between the nonlinear and linear regions of the K-factor and its standard error in the linear region were set as the objective functions for the optimal design process. The improvement in performance of the optimized impeller design was experimentally verified by evaluating water supply prediction errors and these objective functions. For quantitative and qualitative analyses of the improvement factors, fluid-structure interaction (FSI) numerical simulations were conducted by employing 6-degree of freedom (6-DOF) and dynamic mesh deformation techniques. The numerical model was validated through quantitative comparison with measured data, while flow visualization was used to assess qualitative similarity of flow features. The detailed analysis based on the numerical results revealed the physical mechanism causing the observed improvements in terms of torque variation and fluid flow energy driving the rotation of the turbine impeller. The proposed experimental framework, complemented by numerical analysis, is applicable to other turbine meter designs.

Nomenclature

Geometry		General (flow, optimization)	
α	Inlet-nozzle centerline angle [*deg.*]	Q	Volumetric flow rate [L/min]
D_h	Hub diameter [*mm*]	Q_{master}	Volumetric flow rate from master meter [L/min]
D_r	Rotor diameter [*mm*]	Q_{KRISS}	Volumetric flow rate from KRISS standard [L/min]
δ	Tip clearance of the tested design [*mm*]	Q_1	Lowest experimental flow setpoint [L/min]
δ_1	Reference tip clearance of the tested design [*mm*]	K	K-factor, pulse per unit volume [Pulse/L]
θ	Blade setting angle at mid-span [*deg.*]	f	Pulse frequency [Hz]
θ_1	Reference blade angle of the tested design [*deg.*]	$\overline{f_{Num}}$	Mean pulse frequency obtained from numerical simulation [Hz]
z	Number of blades [−]	$\overline{f_{Exp}}$	Mean pulse frequency obtained from experimental [Hz]
w_n	Inlet-nozzle throat width [mm]	Q_c	Threshold flow rate for linear region onset [L/min]
n	Pulse count during time interval [−]	σ	Standard deviation within the identified linear region [−]
N	Pulses per revolution [−]	F_{obj}	Objective function value [−]
		ξ	Gradient threshold used to detect Q_c [−]

(*continued on next column*)

(*continued*)

* Corresponding author. School of Mechanical Engineering, Pusan National University, 46241, Busan, South Korea.
E-mail address: ccheong@pusan.ac.kr (C. Cheong).

https://doi.org/10.1016/j.flowmeasinst.2025.103134
Received 12 March 2025; Received in revised form 9 November 2025; Accepted 21 November 2025
Available online 22 November 2025

1. Introduction

Accurate flow measurement is critical in various industrial applications, including chemical processing, water management, fuel distribution and even home appliances. In recent years, home appliances have evolved to include a range of additional features that enhance their value in daily life. In household refrigerators, functions such as water purification, ice making, and AI integration have become key factors influencing consumer purchasing decisions. Among these, spherical ice-making technology used in home cafés or for chilling whiskey has received increasing attention as a distinctive feature that heightens refrigerator competitiveness.

During ice making, quality issues can occur depending on the size and number of ice pieces and the operating environment, all of which have a direct effect on consumer satisfaction. For spherical ice production in a home refrigerator, the process generally consists of three steps involving water supply, ice formation, and ice release. Accurately controlled water supply is essential for producing high-quality spherical ice, necessitating a flow control system during the water supply stage. The water supply valve is precisely regulated once the flow sensor detects the target flow, and the performance of the flow meter system is crucial to ice quality. In domestic ice maker systems, the water supply process typically operates under low pressure conditions (approximately $0.14 \sim 0.83\,MPa$) and at a nominal flow rate of about $1.9\,L/\ min$, consistent with manufacturer specifications for household refrigerator water lines.

Among the numerous types of flow meters available, each has distinct advantages and limitations depending on the operating conditions and measurement requirements. Common types of flow meters include differential pressure (DP) flow meters, electromagnetic flow meters, ultrasonic flow meters, and turbine flow meters [1]. Differential pressure flow meters, such as orifice plates, Venturi tubes, and Pitot tubes, measure flow rate by inducing a pressure drop across a constriction. These meters are widely used due to their simple design and robustness. However, they suffer from significant pressure losses and require frequent calibration to maintain accuracy. Additionally, their performance is affected by changes in fluid properties such as viscosity and density. Electromagnetic (magnetic) flow meters operate based on Faraday's law of electromagnetic induction, measuring the voltage generated as a conductive fluid passes through a magnetic field. These meters are highly accurate, have no moving parts, and are ideal for measuring the flow of conductive liquids such as water, wastewater, and certain chemicals. However, they are ineffective for non-conductive fluids such as hydrocarbons and gases and tend to be more expensive than other flow measurement solutions. Ultrasonic flow meters use the transit-time or Doppler effect principle to measure flow velocity. These meters offer the advantage of being non-intrusive, as they can be mounted externally without interrupting the flow. They provide high accuracy and low maintenance requirements but can be sensitive to flow disturbances and may not perform well in applications involving low flow rates or aerated fluids.

Turbine flow meters operate by placing a freely rotating turbine in the flow stream, where the rotational speed of the turbine is proportional to the flow rate. These meters are valued for their high accuracy, repeatability, and ability to measure both low and high flow rates with minimal pressure drop. They are particularly well-suited for measuring clean, low-viscosity fluids such as water, fuels, and gases. Due to these merits, turbine flow meters are used in ice-maker water-supply system in household refrigerators. In real applications, a turbine flow meter measures flow rate by detecting pulses generated from the turbine's rotation induced by fluid flow. The water supply volume can be predicted by measuring the rotation speed of the turbine. The measurement accuracy of the flow meter depends on the precision of flow measurement. However, the nonlinear behavior of turbine flow meters under low-pressure conditions frequently results in substantial prediction errors. Accordingly, various studies have evaluated and enhanced the accuracy of turbine flow meters.

Saboohi et al. [2] developed a numerical model to evaluate the performance of helical turbine flow meters, integrating a method that incorporates the influence of bearing friction torque. Using a steady state Moving Reference Frame (MRF) approach in CFD, they analyzed internal flow characteristics, and the model's reliability was validated experimentally using crude oil and water at flow rates between $1{,}000 \sim 9{,}000\,L/min$. Their study demonstrated that the developed model could accurately predict the K-factor and linearity error, confirming its validity under steady industrial conditions. Zhen et al. [3] conducted a comprehensive study on tangential-type turbine flow meters, focusing on theoretical and numerical modeling. They introduced a torque balance analysis method in the rotor's rotation-direction and applied the MRF technique for CFD simulations. Experimental validation on flow calibration facilities demonstrated the effectiveness of their approach, offering valuable insights into the forces acting on tangential-type turbine flow meters and the reliability of K-factor-based performance evaluations. The tests were performed at flow rates of approximately $0.5 \sim 3\,L/min$, representing low-flow conditions. Hariri et al. [4] conducted a numerical study on a 12-inch industrial turbine flow meter, analyzing the effects of flow rate, fluid density, and viscosity using CFD simulations with the Realizable k-ε turbulence model and MRF technique under moderate-flow industrial conditions ($\approx 41 \sim 50\,L/min$). Their results demonstrated that viscosity increases the K-factor, while distorted flows and damaged blades significantly affect measurement accuracy. In terms of optimization, Guo et al. [5] analyzed the effect of fluid viscosity on turbine flow sensor performance through internal flow analysis. They proposed optimizing the ratio of the sensor hub radius to the housing inner radius to reduce viscosity-induced effects on velocity profiles and adjusting the impeller length to minimize leakage flow. CFD simulations and experiments validated the optimized design, demonstrating reduced linearity errors and improved meter factor consistency across a wide viscosity range. Guo et al. [6] proposed a method to enhance the linearity and overall performance of turbine flow sensors by optimizing blade shape parameters, particularly reducing the blade tip area. Using CFD simulations and experimental validation, they demonstrated that structural modifications, such as adjusting blade geometry, effectively minimized linearity error and improved sensor accuracy. This study underscores the significance of design optimization in achieving reliable and efficient turbine flow sensor performance across varying flow conditions. Qu et al. [7] employed the response surface methodology (RSM) to optimize the structural parameters of turbine flow meters, aiming to enhance measurement accuracy and stability in geothermal resource exploration. Significant structural factors were identified using the Plackett–Burman method, followed by detailed optimization through Box–Behnken experiments and CFD simulations. Their analysis underscored the critical influence of blade geometry and other design parameters on reducing linearity error, improving measurement performance, and providing an optimized design solution.

Most previous studies on turbine flow-meter performance and optimization have been conducted under steady or industrial operating conditions, where the impeller speed is prescribed using the Moving Reference Frame (MRF) approach for computational simplicity. Although this framework predicts steady flow features and linear K-factor trends, it assumes a fixed rotational speed and therefore offers limited capability to capture fluid-driven dynamics and rotor–flow coupling that govern nonlinear behavior under low-pressure operation. Optimization studies have primarily focused on overall performance and linearity under steady, high-flow conditions, with low-pressure nonlinear behavior remaining largely unexplored.

To address these limitations, this study employs a fluid-structure interaction (FSI) approach with dynamic mesh (dynamic meshing) technique to accurately simulate fluid-driven impeller motion. The main goal of this study is to improve flow measurement performance by

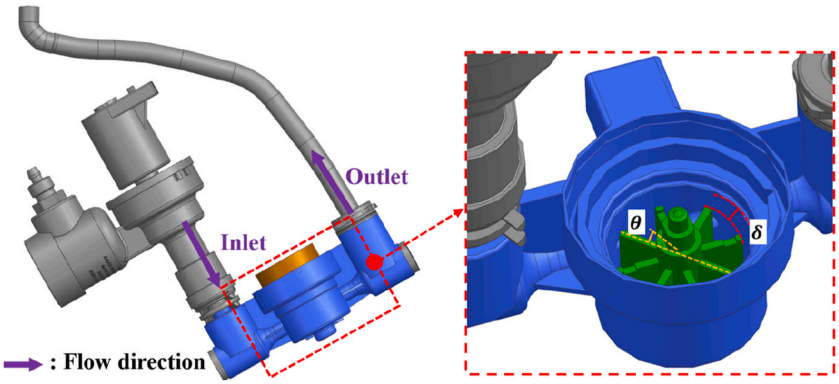

Fig. 1. Geometry of target turbine flow meter.

Table 1
Non-dimensional geometric parameters of target turbine flow meter.

Geometric parameter	value
Hub ratio, D_h/D_r	0.35
Tip clearance ratio, δ_1/D_r	0.11
Blade angle ratio, θ/θ_1	0
Number of blades, z	8
Inlet nozzle width ratio, w_n/D_r	0.20
Inlet nozzle angle, α/θ_1	0

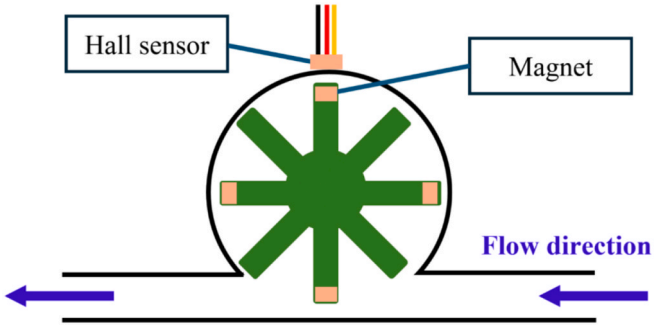

Fig. 2. Cross section of target turbine flow meter.

optimizing the shape of the impeller blades in a turbine flow meter, with a focus on mitigating nonlinear behavior in low-pressure operation. First, an experimental apparatus was built to assess meter performance, and its precision was verified using data from the Korea Research Institute of Standards and Science. A Design of Experiments approach was then used to develop nine experimental models, which were fabricated and tested. Based on the K-Factor frequently used as an important flow meter performance metric, an objective function was defined to minimize the nonlinear region. Through the response surface analysis, the optimized model was found to predict water supply volume more accurately than the baseline model under identical supply conditions. For further investigation into the physical mechanism responsible for this performance improvement, a virtual turbine flow meter (VTFM) based on the computational flow dynamics (CFD) technique in association with the flow-structure interaction simulation was developed and applied. Numerical results obtained from the VTFM were verified using the measured flow rate and experimentally visualized flow structure within the turbine. Finally, the effectiveness of the optimal design was demonstrated by analyzing the torque and energy characteristics of the impeller.

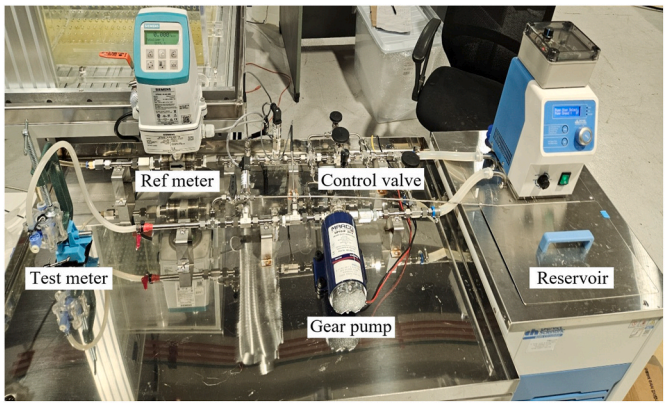

Fig. 3. Experiment facility.

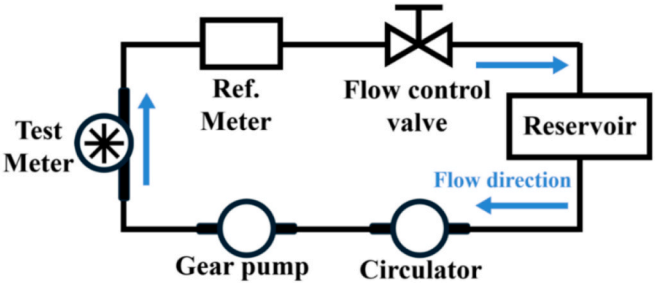

Fig. 4. Diagram of experiment facility.

2. Target turbine flow meter

As shown in Fig. 1, the tangential-type turbine flow meter investigated in this study consists of inlet and outlet pipes, a housing, a cover, and an impeller. The impeller features eight blades arranged such that the flow direction is perpendicular to the rotational axis, and it is enclosed by the housing, cover, and inlet-outlet piping system. Key geometric parameters of the device under test are summarized Table 1. Fig. 2 presents a cross-sectional view of the turbine flow meter, illustrating the mechanism by which pulses are measured through the interaction between magnets attached to the impeller and an external Hall sensor.

Table 2
Specifications of the flow-control and measurement components used in the experimental setup.

Component	Model	Specifications
Thermostatic bath	Digital PID- controlled water bath with PT-100 Ω seonsor	Temperature range: 10 ∼ 40 °C (Control accuracy : ±1°C, Measurement accuracy: ±0.05°C)
Gear pump	MACRO Gear Pump	Max flow: 18 L/min Max pressure: 7 bar Operation temp: 10 ∼ 40 °C
Reference (master) meter	Siemens SITRANS MAG 1100 sensor + MAG 6000 transmitter	Accuracy: ± 0.5% Repeatability: ± 0.2% (KRISS traceable)
Flow control valves	Precision manual globe valves	∅15mm, 4mm, 1.5mm

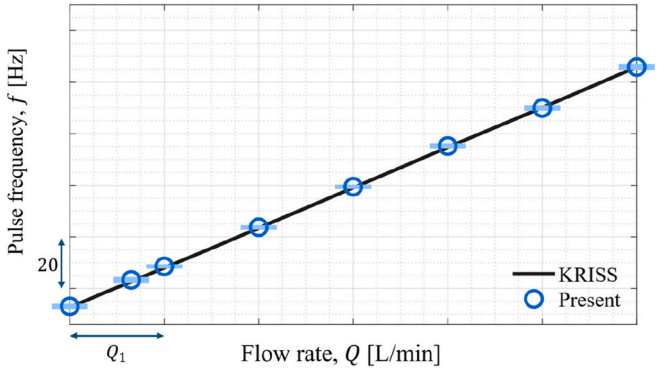

Fig. 5. Pulse frequency-based validation (Turbin flow meter vs KRISS).

3. Experimental and numerical methods

3.1. Experimental method

To evaluate the performance of the turbine flow meter, the experimental apparatus shown in Fig. 3 was designed and constructed. This setup complies with the international standard ISO 17025 [8] and employs the master meter method [9] for accurate flow meter performance assessment. Fig. 4 provides a flow diagram of the setup, illustrating how the pump draws fluid from a reservoir and supplies it to the test section. The apparatus implements the master meter method by operating the test meter and a reference meter simultaneously and correcting measured flow values based on the difference between the two readings. The detailed specifications of the flow control system, reference meter, and other components are summarized in Table 2 for clarity and reproducibility. The experimental range was $Q \in [Q_1, 7Q_1]$, where Q_1 denotes the lowest experimental flow setpoint, using water at 20 $\pm 1°C$ ($density = 998.2\ kg/m^3$, $dynamic\ viscosity = 0.001003\ kg/ms$). Flow rates were finely controlled using the gear pump's angular velocity and precision manual globe valve. At each setpoint, data were recorded after stabilization using 20-s averages, and selected points were repeated to confirm consistency. To ensure the reliability of the apparatus, a commercial turbine flow meter model was tested and validated against data from the Korea Research Institute of Standards and Science (KRISS), which establishes, maintains and improves national measurement standards. The calibration was performed at the KRISS primary standard flow facility under controlled conditions (22 $\pm 1°C$, 50 $\pm$ 5 % RH) over a flow range of $2Q_1 \sim 6Q_1$ with three repeated measurements at each point. The KRISS reference system provided an expanded uncertainty of $\pm$ 0.09 ∼ 0.11 % at the 95% ($coverage\ factor = 2.8$). Fig. 5 demonstrates the reproducibility of the turbine meter, while Fig. 6 verifies the accuracy of the master meter, with deviations within ± 1 % across the tested range, where $Deviation(\%) = 100 \times \frac{|Q_{master} - Q_{KRISS}|}{Q_{KRISS}}$. In both figures, the error bars (vertical: measurement repeatability, ±1 standard deviation and horizontal: KRISS expanded uncertainty at the 95 % confidence level with $coverage\ factor = 2.8$ confirm that both measurement variability and reference uncertainty are sufficiently small for the present study.

3.2. Numerical methods

For the quantitative and qualitative evaluation of the target flow meter system, numerical simulations were performed using the commercial software ANSYS Fluent V2023R1. To model the flow field, the three-dimensional unsteady incompressible Reynolds-Averaged Navier-Stokes (RANS) equations were adopted as the governing equations in the form,

$$\frac{\partial}{\partial x_j}(u_j) = 0 \tag{1}$$

$$\frac{\partial}{\partial t}(u_i) + \frac{\partial}{\partial x_j}(u_j u_i) = g - \frac{1}{\rho_0}\frac{\partial p}{\partial x_i} + \frac{\partial}{\partial x_j}\left(\nu\left(\frac{\partial u_i}{\partial x_j} + \frac{\partial u_j}{\partial x_i}\right) - \overline{u_j' u_i'}\right) \tag{2}$$

here, ρ_0 denotes density, u_i denotes flow velocity, ν denotes kinematic viscosity and p denotes static pressure. Equation (1) represents mass conservation, while Eq. (2) represents momentum conservation.

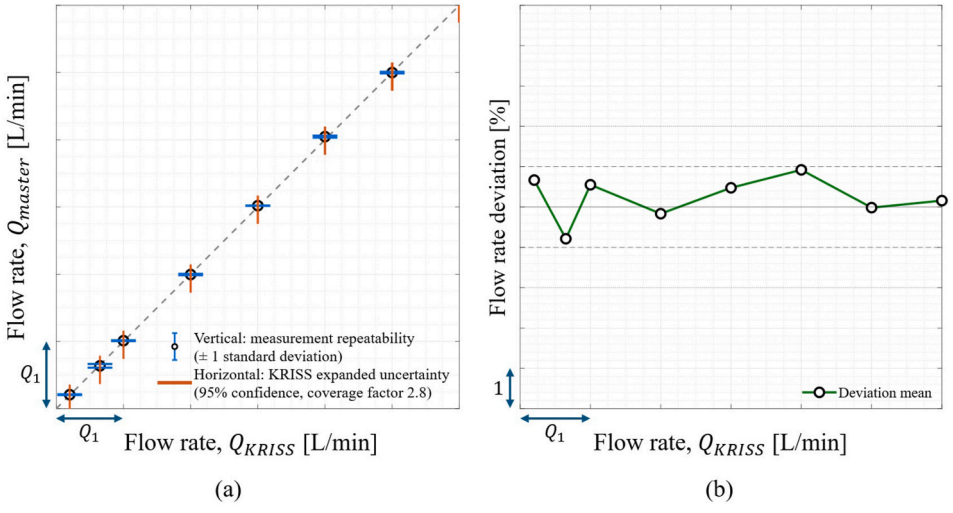

Fig. 6. Flow rate-based validation (Master meter vs KRISS) (a) Flow rate agreement (b) Deviation of flow rate.

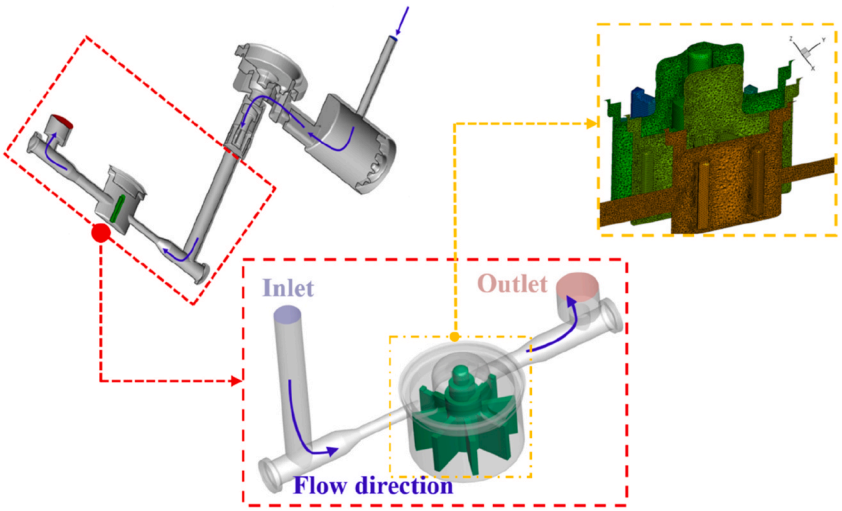

Fig. 7. Computation domain and mesh configuration for the virtual turbine flow meter.

As the turbulence model for the RANS equations, Menter's Shear Stress Transport (SST) k−ω model [10,11] was chosen due to its widespread use and suitability for complex flow phenomena such as boundary layer flows, flow separation and reattachment, and rotating flows. The working fluid was liquid water including gravitational effects. The momentum term was discretized using a second-order upwind scheme; time discretization was performed using a second-order implicit scheme; and the SIMPLE scheme was adopted for the pressure velocity coupling, ensuring computational stability. A fixed time step of 5×10^{-5} s was used after initial stabilization, and convergence at each step was achieved with residuals below 10^{-5} for all governing equations.

Fig. 7 shows the computational domain for the virtual turbine flow meter (VTFM), designed to reflect the actual flow path of the turbine flow meter system. The domain was discretized into approximately 3 million unstructured tetrahedral cells. A single mesh was generated for the entire geometry without separating the rotor and stator regions, as dynamic meshing was employed to capture the impeller motion. The mesh was updated at each time step to maintain quality, with the maximum skewness kept below 0.85. The experimentally measured flow rate was prescribed at the inlet, atmospheric pressure at the outlet, and no-slip boundary conditions were applied to both the impeller and the housing walls. To accurately simulate the rotational motion of the flow meter impeller, a fluid-structure interaction (FSI) method based on dynamic mesh (dynamic meshing) was employed. In most preceding studies, a moving reference frame (MRF) method is applied in rotating flow analyses to assign a constant rotational speed to rotating parts such

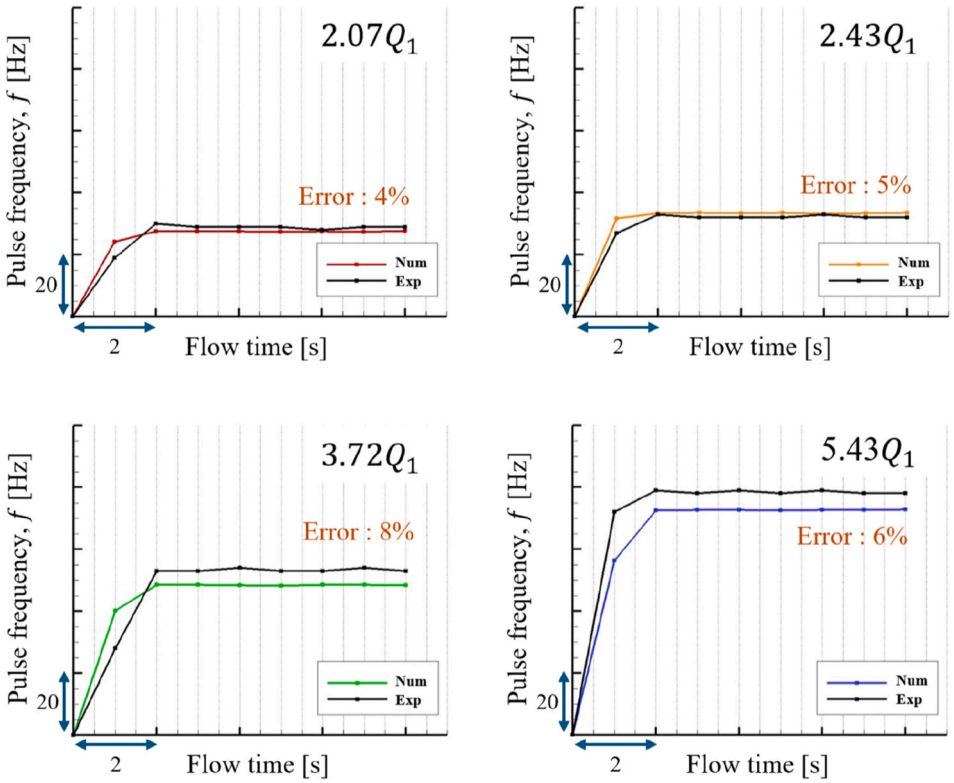

Fig. 8. Comparison of simulated and experimental pulse frequencies for four representative flow rates (2.07 Q_1, 2.43 Q_1, 3.72 Q_1, 5.43 Q_1).

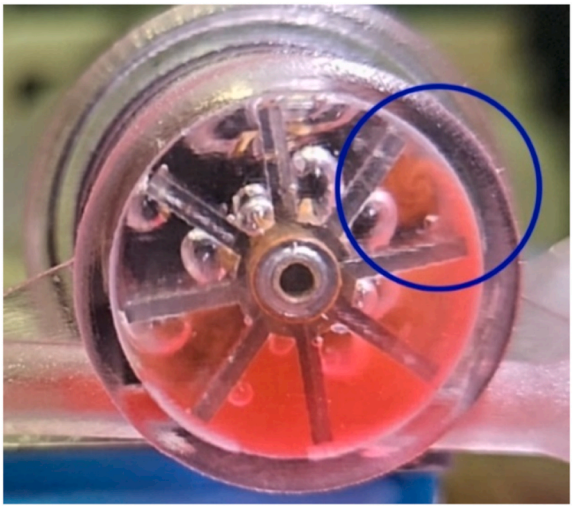

Fig. 9. Snapshot of tip-vortex structure in transient flow field driving impeller rotation.

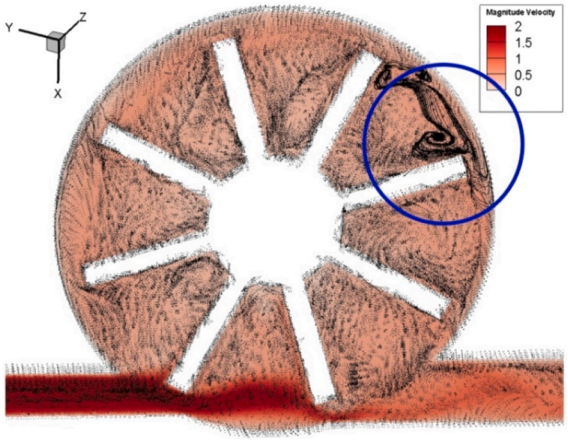

Fig. 10. Snapshot of flow velocity distribution obtained from transient flow simulation.

as fans. However, the turbine flow meter in this study is driven by fluid forces and must be modeled with dynamic rotation, as assuming a fixed rotational speed would be inadequate. Capturing dynamic characteristics such as the impeller's acceleration demands significant computational resources. Therefore, to achieve more accurate simulations, the present study employed a 6-degree of freedom (6-DOF) method combined with a dynamic mesh technique for FSI analyses [12]. The 6-DOF method calculates translational and rotational motion at the center of mass of an object based on forces and moments acting on it [14]. Rotational motion is computed in the object's coordinate system using the following equations:

$$\dot{\vec{\omega}}_B = L^{-1}\left(\sum \vec{M}_B - \vec{\omega}_B \times L\vec{\omega}_B\right) \tag{3}$$

$$\vec{M}_B = R\vec{M}_G \tag{4}$$

$$R = \begin{bmatrix} C_\theta C_\psi & C_\theta S_\psi & -S_\theta \\ S_\phi S_\theta C_\psi - C_\phi S_\psi & S_\phi S_\theta S_\psi + C_\phi C_\psi & S_\phi C_\theta \\ C_\phi S_\theta C_\psi + S_\phi S_\psi & C_\phi S_\theta S_\psi - S_\phi C_\psi & C_\phi C_\theta \end{bmatrix} \tag{5}$$

here, L denotes the inertia tensor, $\vec{\omega}_B$ is the angular velocity, and $\vec{M}_B$ represents the torque acting on the object. Equation (4) converts torque from the inertial coordinate system to the object's coordinate system, while Equation (5) defines the transformation matrix R. The inertia tensor of the impeller was obtained from the CAD model in SpaceClaim by assuming a plastic material with a density of 1.05 g/cm^3. Friction and electromagnetic effects were neglected, as their influence is minor compared with the hydrodynamic torque acting on the impeller. Using the 6-DOF history, the impeller angle $\theta(t)$ was converted to angular velocity $\omega(t)$, pulse frequency f, and K-factor $K = f/Q$. Stationarity was defined by the invariance of K within a prescribed tolerance. Once stationarity was reached, the mean angular velocity $\overline{\omega} = \frac{\sum_{i=1}^{M} \omega_i}{M}$ was used to compute the pulse frequency, $f = \frac{n}{t} = \frac{\overline{\omega}}{2\pi} N$, where N is number of pulses per revolution, and k-factor was evaluated as $K = f/Q$.

The numerical model was then validated against four representative flow rates (2.07 Q_1, 2.43 Q_1, 3.72 Q_1, 5.43 Q_1). Fig. 8 shows close agreement between simulation and experiment, with both transient rise and steady plateaus well reproduced. The relative deviation was defined as

$$Error(\%) = 100\,\frac{\left|\overline{f_{Num}} - \overline{f_{Exp}}\right|}{\overline{f_{Exp}}}$$

And the time-averaged steady pulse frequency $\overline{f_{Num}}$ agreed with the experimental counterpart $\overline{f_{Exp}}$ within 4–8 %. These results confirm that the solver can reliably capture the metrological response of the turbine flow meter, providing confidence for the subsequent optimization and flow-field analysis.

In addition to the frequency-based validation described above, the present numerical approach has also been benchmarked against experiments in a prior study [12]. To further corroborate the model's reliability for the present configuration, qualitative flow visualization was performed using a transparent housing with water soluble dye, and high-speed-camera recordings were obtained [13]. Fig. 9 shows the

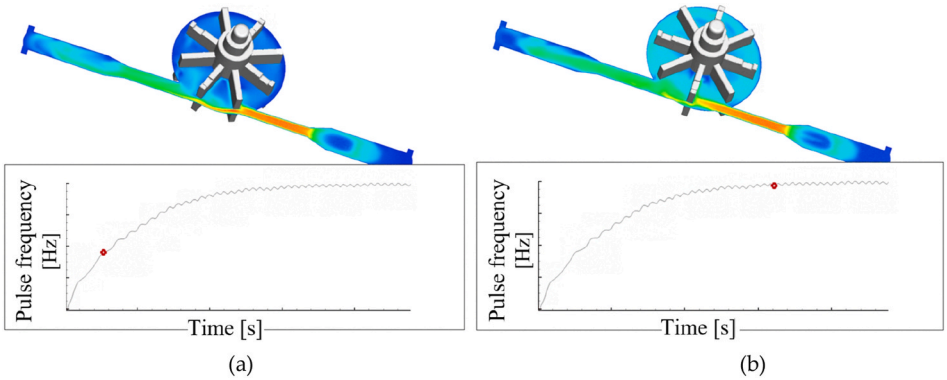

Fig. 11. Time-history of pulse frequency and snapshot of iso-contours of pressure distribution on mid-span plane in(a) initial acceleration and (b) later converged ranges.

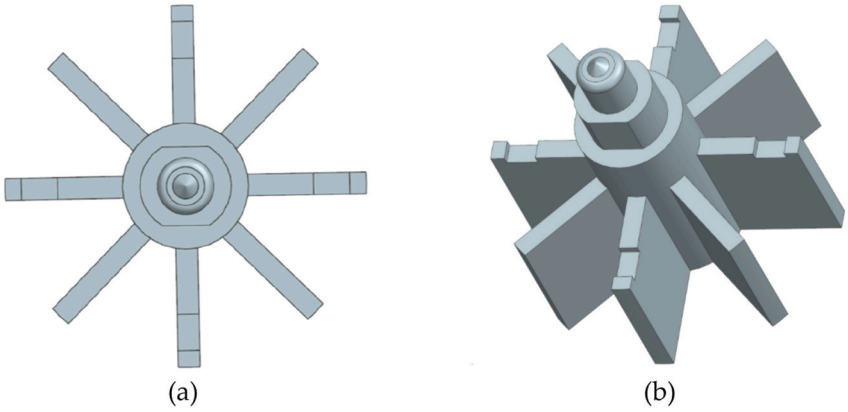

Fig. 12. Original impeller geometry: (a) Top view, and (b) Isometric view.

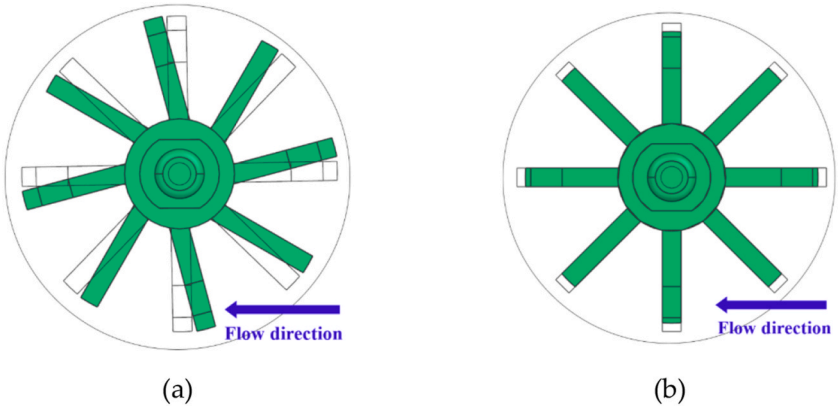

Fig. 13. Design parameters: (a) blade install angle, (b) tip clearance.

results obtained using the transparent housing: the flow passing through the gap between the impeller tip and the housing exits near the tip and contributes to rotor rotation. Fig. 10 presents the corresponding numerical snapshot of velocity magnitude and vectors on a mid-span plane, which also flow turning at the impeller tip and the associated near-tip leakage motion. Although minor differences exist and quantitative evaluation was limited, the observation of near-tip separation and tip–gap leakage in both experiment and simulation provides supplementary qualitative support for the numerical method.

Fig. 11 presents the snapshot of the pressure distribution on the mid-span plane during the transient numerical simulation with the pulse frequency detected at the selected time. In the accelerating region as shown in Fig. 11 (a), the turbine rotational speed is increasing from an initial resting state due to the driving torque of water flow greater than the resistant torque. As the turbine rotation speed increases, the flow resistance also increases and when the flow resistance becomes equal to the driving torque of the water, the turbine speed converges as shown in Fig. 11 (b). This result highlights the potential of the numerical methods enabling precise computation of the pulses generated during operation.

Table 3
Model number (M1–M9) based on design parameters: blade angle θ and tip clearance δ

Blade angle, θ [deg.]	Tip clearance, δ [mm]		
	$0.75\delta_1$	δ_1	$1.25\delta_1$
$2\theta_1$	M1	M2	M3
θ_1	M4	M5	M6
0	M7	M8	M9

4. Optimal design

4.1. Selection of design variables

In this study, to improve flow measurement performance, the impeller blades were chosen as the target for optimal design, as shown in Fig. 12. Although the impeller's operating mechanism differs from that of a typical fan, the flow characteristics are similar to those of a centrifugal fan. Therefore, based on known key performance factors of centrifugal fans and pumps [15–19], the blade angle and tip clearance (the blade-to-housing gap) were selected as the primary design variables.

Fig. 13(a) illustrates one of the two design variables, the blade install angle θ, which is widely recognized as a major factor influencing impeller performance [16–19]. Depending on the blade configuration, impellers can be categorized as forward-type, radial, or backward-type, each exhibiting distinct flow characteristics. In this study, the focus was on maintaining a backward-type blade, angled in the direction of the flow, and varying only its angle as a design variable. Fig. 13(b) shows the other design variable, tip clearance δ, which denotes the gap between the impeller tip and the housing, which is also known as a key factor affecting fan performance [16–19]. This dimension must consider manufacturing tolerances as a design constraint. Based on a two-factor, three-level design of experiments (DOE) using a central composite design, nine models were generated. Table 3 lists these models and their design parameter ranges. For clarity, the impellers in Fig. 14 are labeled with model numbers corresponding to the design variables-blade angle and tip clearance - listed in Table 3. In this context, θ_1 and δ_1 denote reference values employed solely for non-dimensionalization and comparative purposes (see *Nomenclature*).

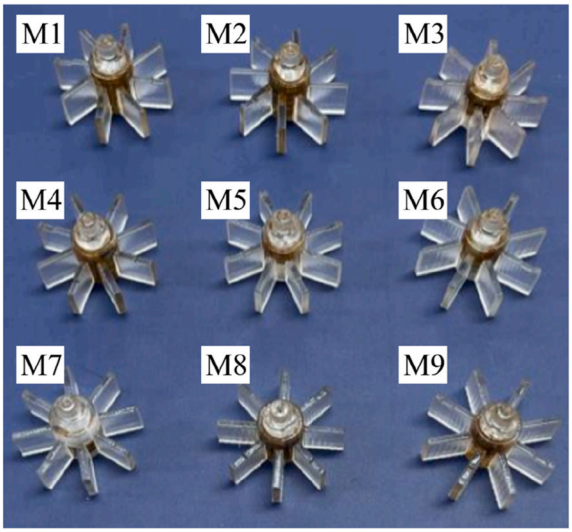

Fig. 14. Experimental samples (M1-M9).

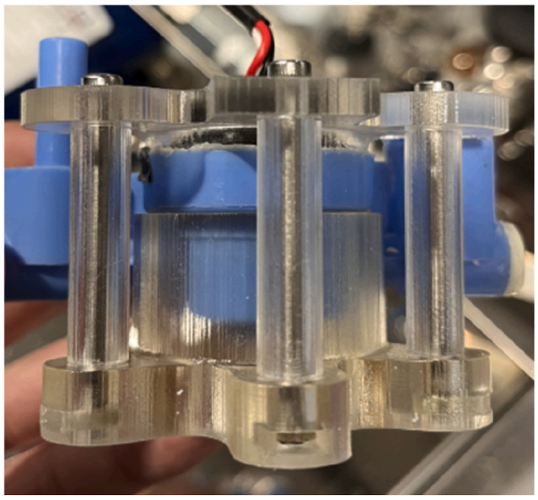

Fig. 15. Housing support.

A total of nine impellers were fabricated according to the design variables, as displayed in Fig. 14. Each model underwent 30 test iterations at intervals of $0.4Q_1$ over the flow range from Q_1 to $7Q_1$, thereby accruing a robust experimental dataset. In addition, to ensure consistent coupling conditions and enhance experimental reliability, a detachable housing support structure was newly developed, as shown in Fig. 15, thereby enabling easy assembly and disassembly of the modified impellers for performance evaluations.

4.2. Definition of objective function

Turbine flow meters exhibit pronounced nonlinear behavior in low-pressure conditions, causing a decline in flow measurement accuracy. To address this issue, an objective function was formulated, as given in the form,

$$Objective\ function, F_{obj} = w(Q_c, \sigma) \times Q_c + \sigma \tag{6}$$

where Q_c represents the flow rate at which the system transitions into the linear region, σ is the standard deviation within the linear region, and $w(Q_c, \sigma)$ is the weighting function. Equation (6) aims to minimize the length of the nonlinear region while simultaneously enhancing stability in the subsequent linear region.

As shown in Fig. 16(a), the K-factor of each impeller model was measured across various flow conditions. A spline function was employed for regression analysis, generating K-factor curves. Fig. 16(b) illustrates how the slope (gradient) of these curves was used to identify the termination point of the nonlinear region via the following equations:

$$Q_c = Q, when \left|\frac{dK}{dQ}\right| = \xi \tag{7}$$

$$\sigma = \sqrt{\frac{1}{n}\sum_{i=1}^{n}(x_i - \overline{x_i})^2} \tag{8}$$

$$w(Q_c, \sigma) = constant : Weighting\ function \tag{9}$$

Let K be the K-factor, Q be the flow rate, and ξ be the threshold gradient value. It can be seen from Equation (7) that the onset of the linear region is determined when the slope of the K-factor curve reaches the threshold value ξ, with the corresponding flow rate Q_c defining its lower boundary. As described by Equation (8), σ denotes the standard deviation within the designated linear region. Since minor fluctuations can still arise in this range, the standard deviation σ was introduced as an additional metric to quantify linear stability. This metric was incorporated into the objective function to ensure stable flow measurement in the linear regime. In addition, to avoid scale-induced dominance between the two terms in Equation (9), each term was first non-dimensionalized by a representative spread computed from the DOE dataset, and the objective was defined as the sum of the normalized terms, thereby ensuring equivalent effective influence. This definition of the objective function balances the influence of flow accuracy and hydraulic loss, thereby stabilizing impeller rotation and consequently reducing nonlinear behavior in the low-pressure regime, resulting in a consistent and physically grounded criterion for evaluating turbine flow meter performance.

4.3. Results of the optimal design

Experimental results and the calculated objective function values for the nine impeller models (ES) designed via DOE are summarized in Table 4. A regression model was then constructed using the following regression equation:

$$Y = \beta_0 + \sum_{i=1}^{2}\beta_i X_i + \sum_{i=1}^{2}\beta_{ii}X_i^2 + \sum_{i=1}^{2}\sum_{j=i+1}^{2}\beta_{ij}X_iX_j + \varepsilon \tag{10}$$

here, Y represents the objective function, which serves as the response variable to be optimized. The coefficients β_0, β_i, β_{ii}, and β_{ij} represent the intercept, linear effects, quadratic effects, and interaction effects, respectively. These coefficients quantify the contributions of individual design variables, their nonlinear relationships, and their interactions to the response. The variables X represent the design parameters, while ε denotes the unexplained error term, accounting for deviations in the response not captured by the regression model. The commercial software Minitab V22 was used to derive the regression model, and the relationship between the design variables and the objective function was expressed via response surface methodology (RSM) [20] in Equation (10). Figs. 17 and 18 provide three-dimensional and two-dimensional pulse maps illustrating how the objective function varies with the blade install angle and tip clearance. The curved response surface demonstrates their coupled influence, where an increased blade angle enhances torque generation while a larger tip clearance promotes leakage loss, resulting in a trade-off region that defines the optimal point. The optimal design point was determined at the minimum of the objective function, and the corresponding values and model are presented in Table 4 and Fig. 19(a).

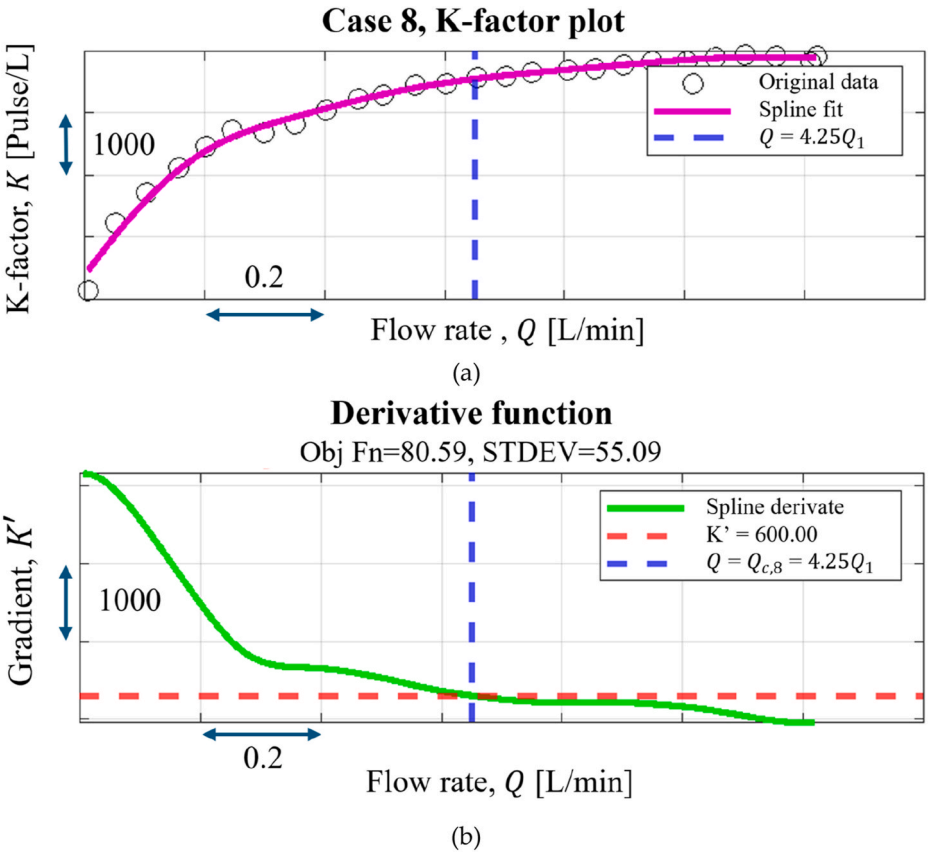

Fig. 16. Case 8 Experiment: (a)K-factor plot, (b)Derivative plot.

Table 4
Results of optimization.

Type	Angle	Tip	Q_c	σ	*Obj Fn*
1	0	$0.75\delta_1$	$3.41Q_1$	90.93	111.4
2	0	δ_1	$4.82Q_1$	40.30	69.22
3	0	$1.25\delta_1$	$4.15Q_1$	61.35	86.27
4	θ_1	$0.75\delta_1$	$4.42Q_1$	76.07	102.6
5	θ_1	δ_1	$3.38Q_1$	28.10	58.41
6	θ_1	$1.25\delta_1$	$4.80Q_1$	48.44	77.24
7	$2\theta_1$	$0.75\delta_1$	$4.25Q_1$	60.70	86.18
8	$2\theta_1$	δ_1	$4.25Q_1$	55.09	80.59
9	$2\theta_1$	$1.25\delta_1$	$3.55Q_1$	57.19	78.46

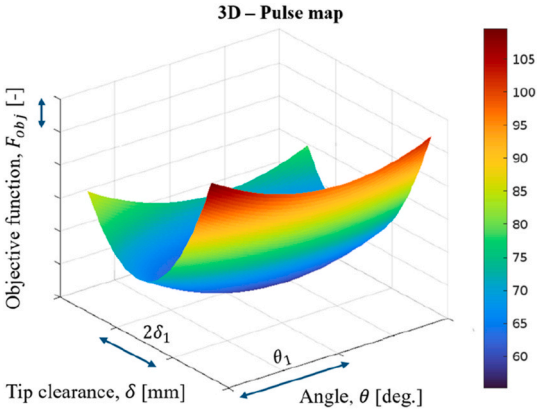

Fig. 17. Three-dimensional Response surface.

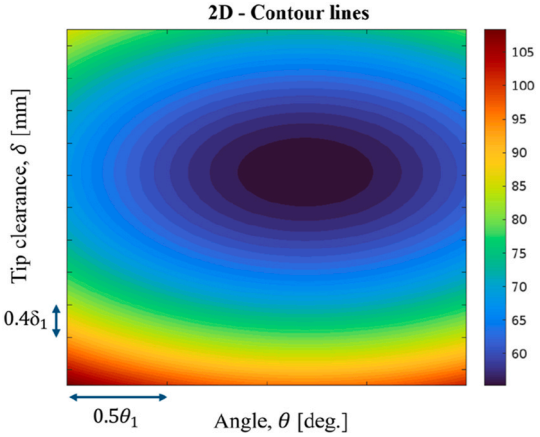

Fig. 18. Two-dimensional Response surface.

4.4. *Experimental validation of the optimal design*

To experimentally verify the proposed optimal design, an impeller based on the optimal model was fabricated, as illustrated in Fig. 19(b), and tested under the same conditions. Fig. 20(a) and (b) depict the K-factor comparisons between the baseline model and the optimized model, covering the entire experimental flow range ($Q_1 \sim 7Q_1$). The optimal model showed a 32 % reduction in Q_c—the flow rate at which the nonlinear region terminates—compared to the baseline. Furthermore, the standard deviation σ in the linear region decreased by 12 %, leading to a 21 % reduction in the objective function value, as summarized in Table 5. Compared with the other DOE candidates, the optimal design reduced Q_c by approximately 25 ~ 35 %, decreased σ

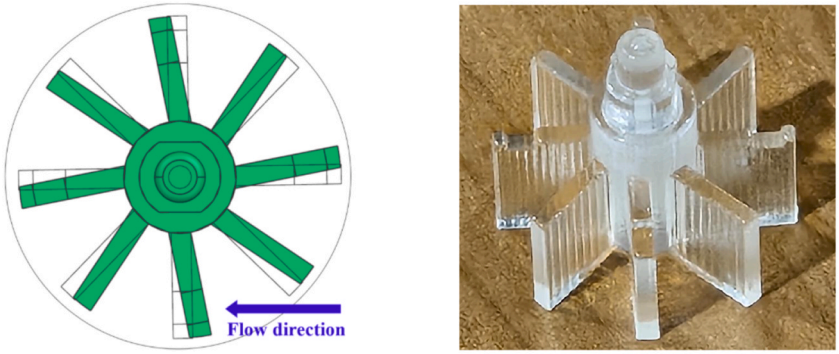

Fig. 19. Optimized design: (a) CAD model, (b) Experiment sample.

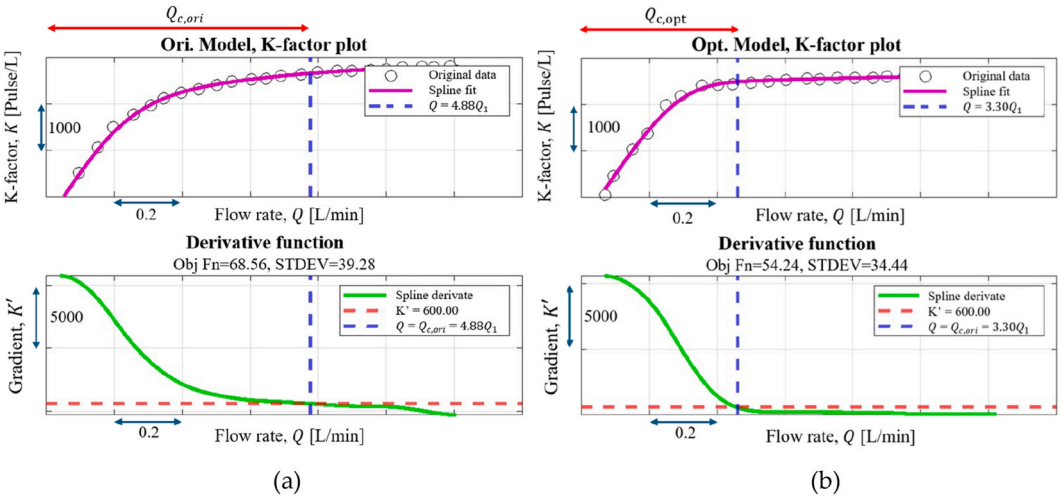

Fig. 20. K-factor plot: (a) Original model, (b) Optimized model.

Table 5
Comparison of original and optimized model.

Type	Blade angle	Tip clearance	Q_c	σ	*Obj Fn*
Original Model	0	δ_1	$Q_{c,cri}$	σ_{ori}	F_{ori}
Optimal Model	$1.1\theta_1$	$1.05\delta_1$	$0.68x_{c,cri}$	$0.86\sigma_{ori}$	$0.79F_{ori}$

within the linear region by 10 ∼ 30 %, and consequently achieved a 15 ∼ 60 % improvement in the objective-function value, confirming its superior linearity and flow-measurement stability across all tested configurations.

At the flow rate $3Q_1$ [L/min] selected in a nonlinear range, the difference between the actual flow rate measured by the reference meter and the predicted flow rate determined from pulse data in the test meter was compared. When the reference meter indicated $3Q_1$ [L/min], the baseline model predicted $2.825Q_1$ [L/min], resulting in a 5.8 % measurement error. In contrast, the optimal model predicted $2.935Q_1$ [L/min] for the same actual flow rate, thereby reducing the error to 2.2 %. This result confirms that the proposed optimal design significantly enhances flow measurement performance in the nonlinear region. The optimization was governed by the coupled relationship between the blade install angle and tip clearance. Increasing the blade install angle enhances torque generation by improving flow incidence, while reducing the tip clearance compensates for leakage sensitivity, forming a multivariable trade-off that defines the optimal design balance in design performance.

5. Analysis of the optimal design

To qualitatively and quantitatively analyze the improvements observed in the optimal model, additional numerical simulations were performed. These simulations provided qualitative visualization of the internal flow field and quantitative evaluation of torque and energy, thereby complementing the experiments and clarifying the mechanism of improvement.

5.1. *Numerical simulation results – qualitative analysis*

Numerical simulations were carried out under specific low-pressure conditions to qualitatively analyze flow characteristics inside the turbine flow meter. Fig. 21 shows the velocity distribution on a cross-section of the flow meter system, illustrating the impeller's rotation driven by the incoming flow. Fig. 21-a and -b present the flow velocity magnitude distribution for the original (baseline) and optimized models, respectively. In the optimized model, the impeller blades are oriented more favorably to the incoming flow, reducing bypass flow. This reduction in bypass flow is identified as a key factor in mitigating the pronounced nonlinear behavior under low-pressure conditions.

Fig. 22 shows the static pressure distribution on a cross-sectional plane of the flow meter system which reveals the working mechanism

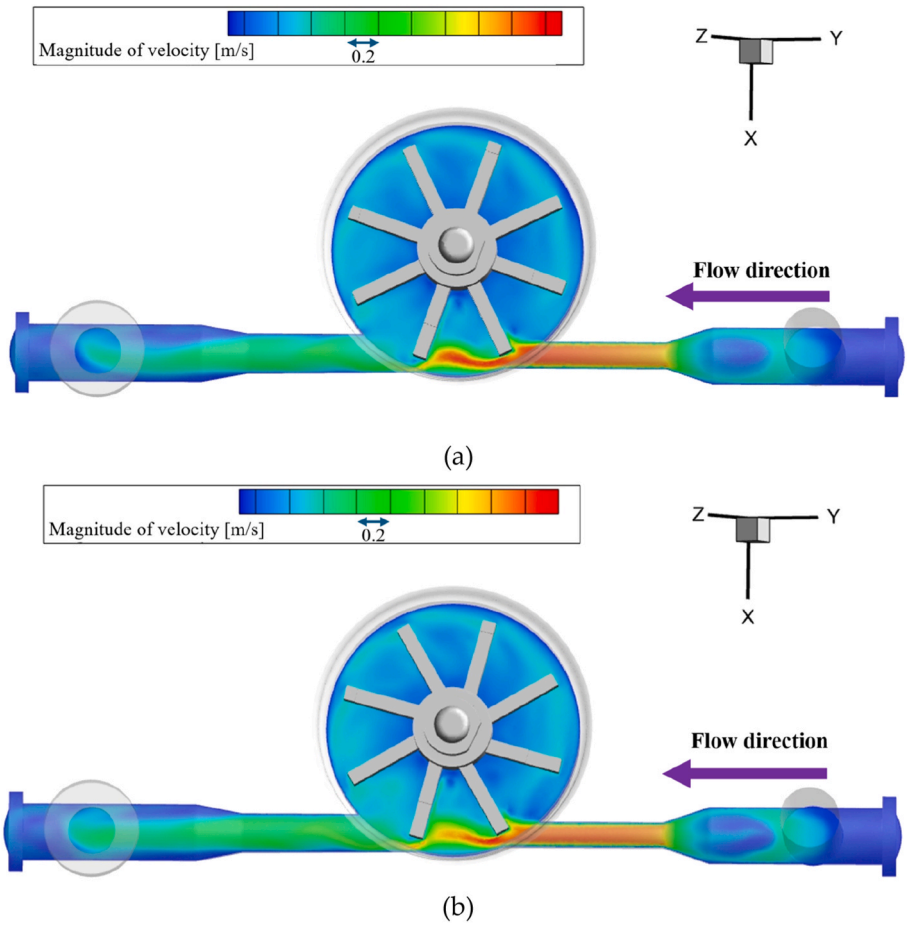

Fig. 21. Velocity magnitude distribution: (a) Original model, (b) Optimized model.

of a turbine flow meter. The incoming flow in an inlet pipe drives the impeller rotation with a pressure difference between the pressure side and the suction side of the blade. A stagnation points forms on the blade's pressure side where the flow first impacts, creating a high-pressure region, whereas the suction side remains relatively low in pressure. Fig. 22-a and b present the results for the baseline and optimized models, respectively, revealing that the suction side of the optimized model exhibits lower static pressure. The backward-type blade configuration in the optimized model helps maintain a larger pressure differential between the two blade surfaces.

To further substantiate this finding, Fig. 23 illustrates the pressure-fluctuation field. In the baseline rotor, alternating positive and negative p' regions are widely distributed near the suction side and tip gap, reducing the effective pressure loading across the blade surfaces. In contrast, the optimized rotor suppresses these unsteady fluctuations, thereby sustaining a more stable pressure difference between the pressure and suction surface. Since this pressure differential generates the driving torque for the impeller, the optimized model achieves a higher driving force and thus superior rotational performance compared with the baseline design.

5.2. Numerical simulation results – quantitative analysis

5.2.1. Torque-based quantitative analysis

Fig. 24 illustrates the time-history of torque acting on the specific impeller blade over two rotation cycles; the orange-highlighted impeller blade. In Fig. 24(a), as the inflow directly collides with the highlighted blade, it generates a significant driving torque, initiating a phase where the incoming flow contributes positively to the blade's rotational motion. In contrast, Fig. 24(b) depicts the resistance torque that increases as the blade transitions out of the inflow region and encounters drag, representing a phase dominated by opposing forces. This periodic pattern demonstrates how the incoming flow creates a driving force during specific intervals, followed by increasing resistance in the ensuing rotation, ultimately producing recurring torque fluctuations throughout the cycle.

Fig. 25 compares the torque distribution over one rotation cycle between the baseline and optimized models. The blue curve, representing the optimized model, exhibits a higher overall driving torque compared to the red curve, which corresponds to the baseline model. This higher torque arises from the increased blade install angle, which improves the attack angle of the incoming flow and strengthens the pressure difference between the pressure and suction sides of the blade, while the reduced tip clearance minimizes leakage loss near the tip. These combined effects result in a greater and more stable driving torque throughout the rotation cycle.

5.2.2. Flow-energy-based quantitative analysis

As shown in Fig. 26, the interior of the housing was defined as the control volume for calculating flow energy based on fluid entering and exiting at the inlet and outlet. Using the measured pressure and flow data at the inlet and outlet, the flow energy was evaluated by the following equation:

$$E = \int_0^T (\Delta p \times Q) dt \tag{11}$$

here, Δp is the pressure difference between the inlet and outlet, and Q is the flow rate at that moment. The product of pressure difference and flow rate yields the fluid power used to rotate the turbine impeller.

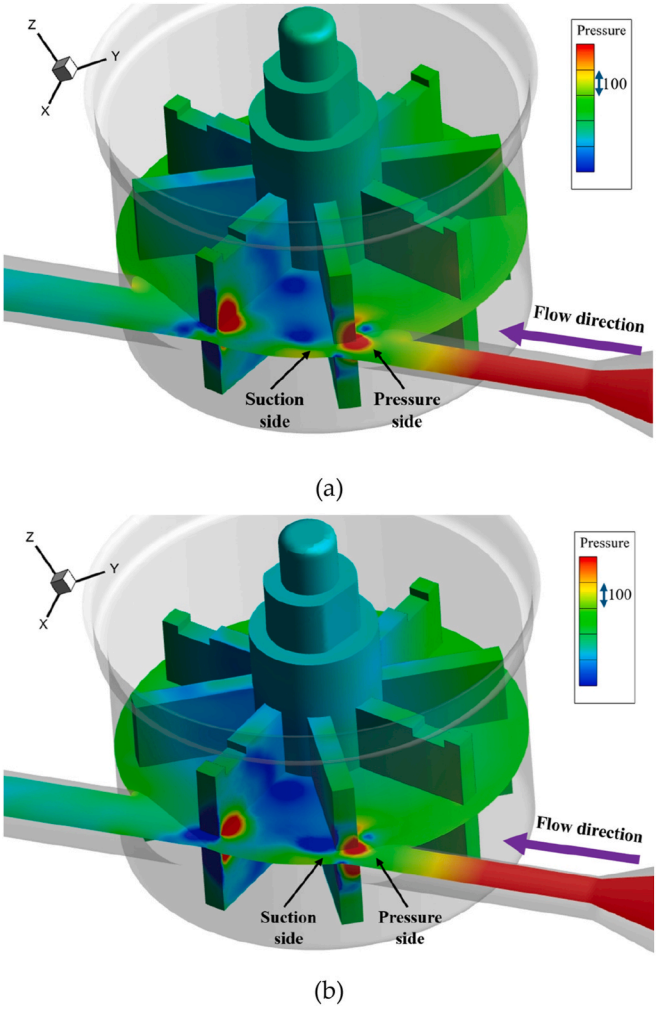

Fig. 22. Iso-contours of static pressure: (a) Original model, and (b) Optimized.

Fig. 27 displays the changes in power over one cycle for both the baseline and optimized models; the time-integration of these curves over one cycle provides the total flow energy. Flow energy represents the mechanical work transferred from the fluid to the impeller, and a higher energy level indicates more efficient conversion of hydraulic power into rotational motion. Compared to the baseline design, the optimized model exhibited a 5.3 % increase in flow energy, confirming the generation of stronger rotational forces.

6. Conclusion

This study focused on improving the flow measurement performance of a turbine flow meter system used for supplying water in refrigerator ice makers. The angle and tip clearance of the impeller blades were selected as design variables, and an optimal design procedure was performed. The results were experimentally and numerically verified and analyzed.

First, an experimental apparatus based on the master meter method was developed to evaluate the flow meter's performance. Its accuracy

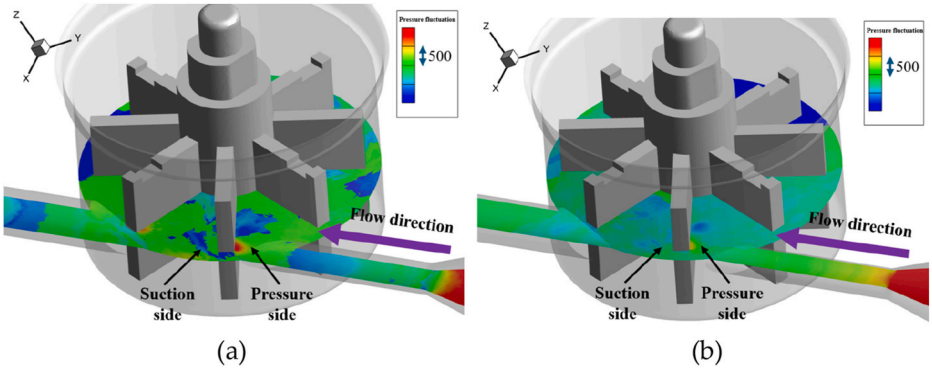

Fig. 23. Iso-contours of Pressure-fluctuation: (a) Original model, and (b) Optimized Model.

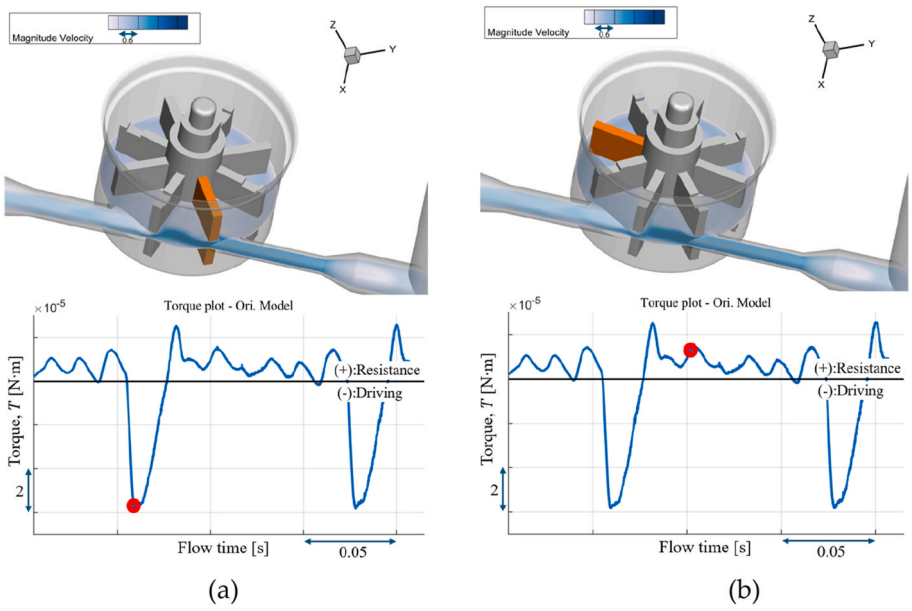

Fig. 24. Distribution of velocity magnitude iso-contours at mid-span cross-sectional plane and time-variation of torque which the colored blade experiences during two rotations: Snapshot in (a) driving phase and (b) resistance range.

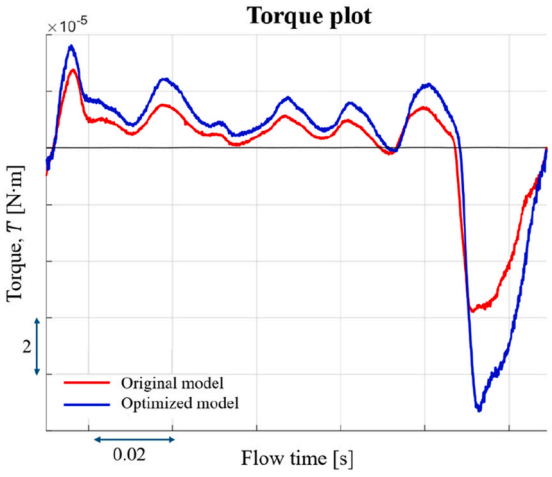

Fig. 25. Comparison of torque: Original model (Red), Optimized model (Blue).

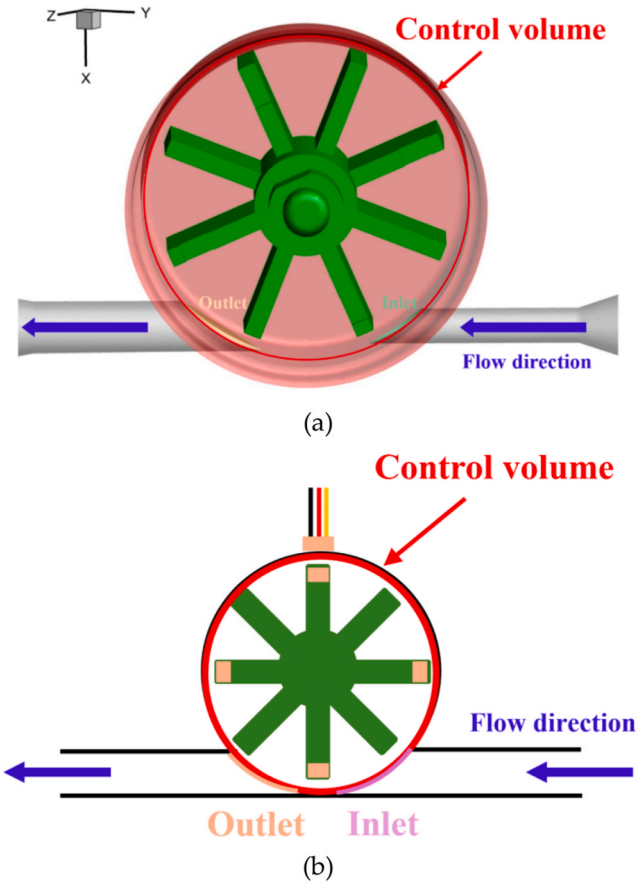

Fig. 26. Control volume of housing: (a) CAD-based view, and (b) Schematic view.

was confirmed via comparisons with measured data from the Korea Research Institute of Standards and Science. Additionally, flow visualization of the internal flow within the turbine meter provided direct observation of the rotational flow. Dynamic mesh deformation and a six-degrees-of-freedom (6-DOF) approach were applied in fluid-structure interaction (FSI) simulations, corroborating the reliability of the numerical method. Together, these methods established a comprehensive approach for evaluating and analyzing turbine flow meter performance.

A key objective was to reduce the nonlinear region under low-pressure conditions and stabilize the linear regime. An objective function was defined for this purpose, and the optimal design identified by this function was experimentally validated. Compared to the baseline, the optimized design reduced the objective function value by 21 % and improved flow measurement accuracy by lowering the difference between actual flow and predicted flow from 5.8 % to 2.2 %. Numerical results showed that the optimized design consumed approximately 5.3 % more energy, thereby inducing stronger rotational forces under low-pressure conditions at the same flow rate. These findings demonstrate that reducing the nonlinear regime and increasing momentum through a lager blade install angle and controlled tip clearance enhance pressure loading and stability, thereby improving flow measurement accuracy under low pressure conditions. Although this study optimized a tangential-type meter within a limited design space, the same K-factor–based evaluation/optimization framework extends to twisted/swept

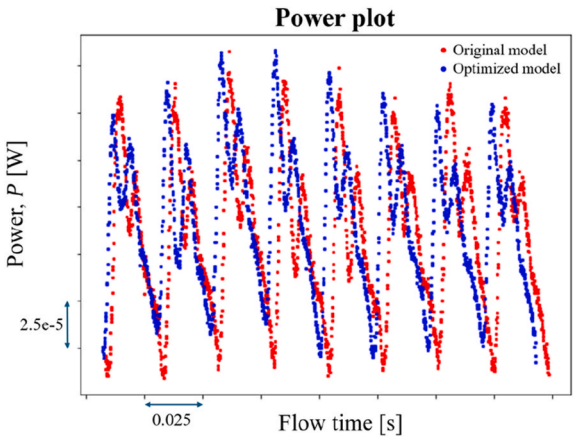

Fig. 27. Comparison of power: red-dotted line: Original model, and blue-dotted line: Optimized model.

rotors [21] and double-rotor layouts [22]. By establishing both the performance evaluation technique and an optimal design and analysis method for turbine flow meters, this study presents a pathway to improving the overall design efficiency of turbine flow meters.

CRediT authorship contribution statement

Haechan Kim: Writing – original draft, Validation, Methodology, Investigation, Formal analysis. **Cheolung Cheong:** Writing – review & editing, Supervision, Methodology, Investigation, Funding acquisition, Formal analysis, Conceptualization. **Seo-Yoon Ryu:** Methodology. **Su Il Park:** Resources, Project administration.

Declaration of generative AI and AI-assisted technologies in the manuscript preparation process

During the preparation of this work the authors used ChatGPT (OpenAI) in order to check the grammatical accuracy of English expressions only. After using this tool/service, the authors reviewed and edited the content as needed and take full responsibility for the content of the published article.

Declaration of competing interest

The authors declare that they have no known competing financial interests or personal relationships that could have appeared to influence the work reported in this paper.

Data availability

The authors do not have permission to share data.

References

[1] R.C. Baker, Flow Measurement Handbook: Industrial Designs, Operating Principles, Performance, and Applications, Cambridge University Press, 2000.
[2] Z. Saboohi, S. Sorkhkhah, H. Shakeri, Developing a model for prediction of helical turbine flowmeter performance using CFD, Flow Meas. Instrum. 42 (2015) 47–57.
[3] W. Zhen, Z. Tao, Computational study of the tangential type turbine flowmeter, Flow Meas. Instrum. 19 (5) (2008) 233–239.
[4] S. Hariri, S.H. Hashemabadi, S. Noroozi, A. Rostami, Analysis of operational parameters, distorted flow and damaged blade effects on accuracy of industrial crude oil turbine flow meter by CFD techniques, J. Petrol. Sci. Eng. 127 (2015) 318–328.
[5] S. Guo, Z. Yang, F. Wang, N. Zao, X. Li, Optimal design of wide viscosity range turbine flow sensor based on flow field analysis, Flow Meas. Instrum. 79 (2021) 101909.
[6] S. Guo, Z. Tao, S. Linjun, Y. Zehn, Y. Wenliang, Blade shape optimization of liquid turbine flow sensor, Trans. Tianjin Univ. 22 (2) (2016) 144–150.
[7] J. Qu, Q. Xue, J. Wang, J. Sun, J. Li, Optimization of a turbine flow well logging tool based on the response surface method, Machines 11 (4) (2023) 455.
[8] ISO 17025, General requirements for the competence of testing and calibration laboratories, Proc. Require. 2017 (2017).
[9] ISO 4185, Measurement of liquid flow in closed conduits, Weigh. Method (1980).
[10] F. Menter, Zonal two equation k–w turbulent models for aerodynamic flows, in: Proc. AIAA Fluid Dynamic Conf., 1993, pp. 1–21.
[11] F.R. Menter, Two-equation eddy-viscosity turbulence models for engineering applications, AIAA 32 (1994) 1598–1605.
[12] S.Y. Ryu, Y.D. Gyu, H.C. Kim, C. Cheong, S.I. Park, Development of numerical and experimental performance evaluation techniques for high-reliability turbine flow meters of ice-making water-dispenser, AIP Adv. 17 (2024) 0753507.
[13] Y. Kim, O. Nematollahi, H.D. Kim, K.C. Kim, Quantitative visualization of the mixing characteristics of a multilayer static mixer by planner laser-induced fluorescence, J. Visual 24 (2021) 671–681.
[14] 2023R1 Ansys Fluent Theory Guide, vol 15317, Ansys Inc., USA, 2023, pp. 85–86.
[15] P.B. Frank, Fan Handbook, McGraw-Hill Inc., New York, 1998, 7.1–7.58.
[16] Y. Song, S.-Y. Ryu, C. Cheong, T.-H. Kim, J. Koo, Optimization of impeller blade shape for high-performance and low-noise centrifugal pump, J. Acoust. Soc. Kr. 42 (2023) 519–528.
[17] M. Jung, J. Choi, S.-Y. Ryu, C. Cheong, T.-H. Kim, J. Koo, Improvement in flow and noise performance of backward centrifugal fan by redesigning airfoil geometry, J. Acoust. Soc. Kr. 40 (2021) 555–565.
[18] J. Choi, S.-Y. Ryu, C. Cheong, M.K. Kim, K.H. Lee, "Blade shape optimization of centrifugal fan for improving performance and reducing aerodynamics noise of clothes dryer", J. Acoust. Soc. Kr. 38 (2019) 321–327.
[19] S. Lee, S. Heo, C. Cheong, Prediction and reduction of internal blade-passing frequency noise of the centrifugal fan in a refrigerator, Int. J. Refrig. 33 (6) (2010) 1129–1141.
[20] R.H. Myers, D.C. Montgomery, Response Surface Methodology, Wiley, New York, 1995.
[21] Zhipeng Ren, Weixing Zhou, Deyou Li, Response and flow characteristic of a dual-rotor turbine flowmeter, Flow Meas. Instrum. 83 (2022) 102120.
[22] Zhipeng Ren, Weixing Zhou, Deyou Li, Investigation on pressure fluctuations of dual – and analogical single-rotor turbine flowmeters, Proc. IME C J. Mech. Eng. Sci. 236 (2022) 13.